Modulation of the Oceanic Mesoscale Activity by the Mesoscale Thermal Feedback to the Atmosphere

LIONEL RENAULT,[a] S. MASSON,[b] V. OERDER,[c,d,e] F. COLAS,[b] AND J. C. MCWILLIAMS[f]

[a] *LEGOS, Université de Toulouse, CNES-CNRS-IRD-UPS, Toulouse, France*
[b] *Sorbonne Universites (UPMC, Univ Paris 06)-CNRS-IRD-MNHN, LOCEAN, Paris, France*
[c] *Escuela de Ciencias del Mar y Instituto Milenio de Oceanografia, Pontificia Universidad Catolica de Valparaiso, Valparaiso, Chile*
[d] *Departamento de Oceanografía, Facultad de Ciencias Naturales y Oceanográficas, Universidad de Concepción, Concepción, Chile*
[e] *Instituto Milenio de Oceanografia, Universidad de Concepción, Concepción, Chile*
[f] *Department of Atmospheric and Oceanic Sciences, University of California, Los Angeles, Los Angeles, California*

ABSTRACT: Ocean mesoscale thermal feedback (TFB) is the influence of mesoscale sea surface temperature (SST) anomalies on the overlying atmosphere and its feedback to the ocean. Over the past few decades, TFB has been shown to affect the atmosphere by inducing low-level wind and surface stress anomalies and modulating ocean–atmosphere heat fluxes ubiquitously over the global oceans. These anomalies can alter the climate variability. However, it is not clear yet to what extent heat and momentum flux anomalies modulate the mesoscale ocean activity. Here, using coupled ocean–atmosphere mesoscale simulations over a realistic subtropical channel centered on the equator in which the TFB can be turned off by spatially smoothing the SST as seen by the atmosphere, we show that TFB can damp the mesoscale activity, with a more pronounced effect near the surface. This damping appears to be sensitive to the cutoff filter used: on average, the surface mesoscale activity is attenuated by 9% when smoothing the SST using an ~1000-km cutoff but by only 2% when using an ~350-km cutoff. We demonstrate that the mesoscale activity damping is primarily caused by a sink of available eddy potential energy that is controlled by the induced-anomalous heat fluxes, the surface stress anomalies having a negligible role. When TFB is neglected, the absence of sink of potential energy is partly compensated by a more negative eddy wind work. We illustrate that TFB filtering in a coupled model must be done carefully because it can also impact the large-scale meridional SST gradients and subsequently the mean large-scale wind stress curl and ocean dynamics.

KEYWORDS: Atmosphere–ocean interaction; Ocean circulation; Ocean dynamics; Coupled models; Mesoscale models

1. Introduction

Mesoscale eddies (i.e., scales from tens to hundreds of kilometers and from tens to hundreds of days; e.g., Wunsch and Stammer 1995; Stammer 1997; Chelton et al. 2007; McWilliams 2008) are ubiquitous in the ocean. They are generated by dynamical instabilities of the large-scale currents and are crucial to understand as they lead to large heat and biogeochemical material transport, modulate the biological production (Martin and Richards 2001; McGillicuddy et al. 2007; Gruber et al. 2011; Renault et al. 2016a; Kessouri et al. 2020), and have an influence on the mean circulation through eddy mean flow interactions (McWilliams 2008; Kang and Curchitser 2015; Renault et al. 2019b) and on the climate (Minobe et al. 2008).

For the past few decades, the mesoscale feedback of the ocean to the atmosphere has been studied, focusing primarily on thermal feedback (TFB) and current feedback (CFB) (e.g., Chelton et al. 2004, 2007; Park et al. 2006; Cornillon and Park 2001; Duhaut and Straub 2006; Dewar and Flierl 1987; Hughes and Wilson 2008; Eden and Dietze 2009; Desbiolles et al. 2014; Ma et al. 2016; Oerder et al. 2016). CFB represents

the influence of surface currents on the overlying atmosphere and its feedback to the ocean. It directly modifies the surface stress (Bye 1985; Kelly et al. 2001; Chelton et al. 2001) and has a bottom-up effect on the wind: a negative current anomaly induces a positive stress anomaly and, thus, a negative wind anomaly (Renault et al. 2016b, 2018, 2019c; Renault and Marchesiello 2022). At the mesoscale, CFB mainly affects the stress and then the wind curl but not their divergence because mesoscale ocean currents are very nearly geostrophic and mainly nondivergent (O'Neill et al. 2003; Chelton et al. 2004; Renault et al. 2016b; Oerder et al. 2018; Renault et al. 2019c). From an oceanic perspective, on the large scale, the alteration of surface stress reduces the mean energy input from the atmosphere to the ocean, slowing down the mean circulation (Pacanowski 1987; Luo et al. 2005; Renault et al. 2016a). At the mesoscale, surface stress curl anomalies induce additional Ekman pumping and, overall, the so-called "eddy killing," that is, a momentum transfer from mesoscale eddies to the atmosphere. Eddy killing causes a damping of the mesoscale activity by about 30% (Renault et al. 2016b,a, 2017b; Oerder et al. 2018; Renault et al. 2019b; Jullien et al. 2020; Renault et al. 2021), which leads to a reduction in the eddy–mean flow interaction and a subsequent stabilization of western boundary currents (Renault et al. 2016a, 2017b, 2019b).

TFB represents the influence of sea surface temperature (SST) gradients and anomalies on the overlying atmosphere and its feedback to the ocean. At the mesoscale, TFB has

been shown to have a large influence on atmospheric variability. TFB has two main local direct effects. On the one hand, it modifies the atmospheric boundary layer turbulence and the wind and consequently modifies the surface stress (see, e.g., Fig. 3 of Chelton et al. 2007). Many studies have shown that TFB has a linear effect on the stress and on the curl, divergence, and magnitude of the wind (Small et al. 2009; O'Neill et al. 2003; Chelton et al. 2004; Chelton and Xie 2010; Desbiolles et al. 2016; Oerder et al. 2016; Renault et al. 2019c). Small et al. (2008) and Seo et al. (2023) provide a review of the different processes involved. On the other hand, the mesoscale TFB alters turbulent heat and moisture fluxes (Kirtman et al. 2012), energizing and anchoring the major storm tracks (Foussard et al. 2019; Czaja et al. 2019), affecting atmospheric properties up to the troposphere (Minobe et al. 2008), and modulating precipitation in the tropics (Kirtman et al. 2012) and over the southern Africa (Desbiolles et al. 2018). From an oceanic perspective, the TFB induced stress anomalies do not generate significant energy transfer from mesoscale eddies to the atmosphere because they are not spatially coherent with surface currents (Renault et al. 2019c). TFB curl stress anomalies also give rise to additional linear and nonlinear Ekman pumping in the ocean, which may have an influence on the baroclinic energy conversion and, hence, the mesoscale activity. Heat flux anomalies can also affect the eddy available potential energy (EAPE) (von Storch et al. 2012; Ma et al. 2016; Bishop et al. 2020), also altering baroclinic energy conversion and, thus, the mesoscale activity. Seo et al. (2016), for the California Current system, suggest that the mesoscale TFB primarily affects eddy propagation without affecting eddy amplitude. In contrast, Ma et al. (2016) suggest that the mesoscale TFB, through the associated heat flux anomalies, damps the mesoscale activity, altering the characteristics of the Kuroshio western boundary current. This apparent contradiction may be related to the definition of the mesoscale activity. Whereas Seo et al. (2016) spatially smooth out the SSTs sent to the atmosphere using a spatial filter with a cutoff of ~300 km, Ma et al. (2016) use a cutoff of ~1000 km. To our knowledge, to date, there is no clear answer on the extent to which TFB can affect oceanic mesoscale activity.

To resolve this puzzling contradiction, in this study, a set of several realistic eddy-rich ocean ($dx = 1/12°$) and atmosphere ($dx = 1/4°$) coupled simulations are performed over a realistic subtropical channel centered on the equator (45°S–45°N) (Samson et al. 2017; Renault et al. 2019c, 2020; Jullien et al. 2020) for a 5-yr period. The simulations include or do not include the mesoscale TFB and the CFB (see section 2). Based on these simulations, the objectives of this study are to assess the extent to which mesoscale TFB modulates mesoscale activity and to determine the primary mechanisms involved. The paper is organized as follows: the models and method are described in section 2. In section 3, the effect of TFB on mesoscale activity is evaluated. Section 4 addresses the main mechanisms involved, while section 5 focuses on the large-scale response. The results are discussed and summarized in section 6.

2. Model and methods

a. Coupled ocean–atmosphere model

The numerical models and configurations are the same as those employed in Samson et al. (2017) and Renault et al. (2019c). The following model descriptions are derived from these studies with minor modifications. We also refer the reader to Renault et al. (2019c) for a detailed description. The ocean simulations are performed with the Nucleus for European Modeling of the Ocean (NEMO) v3.4 (Madec and NEMO Team 2015). The atmospheric component is Weather Research and Forecasting (WRF) Model, version 3.3.1 (Skamarock et al. 2008). NEMO and WRF are coupled through the OASIS3-MCTV3 coupler (Craig et al. 2017).

The geographic domain is a realistic subtropical channel centered on the equator and extending from 45°S to 45°N, with the oceanic grid (at 1/12°) being a perfect subdivision by 3 of the atmospheric grid (at 1/4°). The vertical ocean grid has 75 levels, with 25 levels above 100 m and a resolution of 1 m at the surface. The atmospheric grid has 60 eta levels, with a top of the atmosphere located at 50 hPa. The WRF default vertical resolution has been multiplied by three below 800 hPa. Around 33 levels are located below 500 hPa with the first eta base level at ~10 m.

The model configuration was set up with the following parameterizations: the longwave Rapid Radiative Transfer Model (RRTM; Mlawer et al. 1997), the Goddard shortwave (SW) radiation scheme (Chou and Suarez 1999), the WSM6 microphysics scheme (Hong and Lim 2006), the Betts–Miller–Janjić (BMJ) convection scheme (Betts and Miller 1986; Janjić 1994), the Yonsei University (YSU) planetary boundary layer scheme (Hong et al. 2006), and the unified Noah land surface model (LSM) with the surface layer scheme from MM5 (Chen and Dudhia 2001). WRF lateral boundary conditions are prescribed from the European Centre for Medium-Range Weather Forecasts ERA-Interim 0.75° resolution reanalysis (Dee et al. 2011) at 6-hourly intervals. The integration of the surface current in YSU is available in WRF following Renault et al. (2019a).

The ocean physics used in NEMO corresponds to the upstream-biased scheme (UBS; Shchepetkin and McWilliams 2009) advection for the tracers and the dynamics with no explicit diffusivity and viscosity. The vertical eddy viscosity and diffusivity coefficients are computed from a TKE turbulence closure model (Blanke and Delecluse 1993). The oceanic open boundary conditions are prescribed with an interannual global 1/4° DRAKKAR simulation (Brodeau et al. 2010). We spun up the oceanic mesoscale circulation, at limited coast, by running a 5-yr forced ocean simulation initialized from 1/4° DRAKKAR simulations.

b. Spatial filtering

Following, for example, Putrasahan et al. (2013), Seo et al. (2016), and Renault et al. (2019c), in some of our sensitivity experiments, we use a spatial Gaussian filter to isolate mesoscale anomalies from the large-scale signal. To limit the computational cost, the SST of the 1/12° ocean model is first

TABLE 1. Gaussian filter characteristics.

σ used at $\frac{1}{4}°$	Smoothing window size			Cutoff wave number (km^{-1})			
	Grid points	km at 0°	km at 45°	−3 dB at 0°	−3 dB at 45°	−10 dB at 0°	−10 dB at 45°
3	18	500	350	1/630	1/442	1/345	1/244
4	25	675	475	1/840	1/590	1/460	1/325
8	49	1340	950	1/1675	1/1185	1/920	1/650
12	73	2005	1420	1/2515	1/1780	1/1380	1/975

interpolated onto the $\frac{1}{4}°$ atmospheric grid using a simple average over the 3×3 ocean cells directly located below each atmospheric cell. The spatial Gaussian filter is then applied to the $\frac{1}{4}°$ SST. In practice, the addresses and weights used in these two steps are merged into a single set that is provided to the coupler to perform the exchange of the SST from the ocean to the atmosphere. The ocean grid points over land are excluded from the calculation, and the interpolation weights are therefore renormalized with the remaining points.

The Gaussian weights of the points located at a distance greater than 3σ are considered as zero. The Gaussian filter is thus applied only on a window $(6\sigma + 1) \times (6\sigma + 1)$. Following the mathematical properties of the Gaussian filter, we can define an analytical expression of the cutoff spatial frequency (wavenumber): $\nu_c = \sqrt{\ln(c)}/(2\pi\sigma d_x)$ where $1/c$ is the cutoff value (the Gaussian filter response is divided by c in the power response), d_x is the spatial resolution (km), and ν_c is the cutoff wavenumber (km^{-1}).

Table 1 summarizes the characteristics of the different Gaussian filters we used ($\sigma = 3, 4, 8,$ or 12), for two different cutoff values (0.5 or −3 dB and 0.1 or −10 dB), at the equator or at 45°. Note that there is a small error in the Renault et al. (2020) (their cutoff wavenumbers must be divided by $\sqrt{2}$), which explains the differences we have in the cutoff wavenumber values for the same Gaussian filter ($\sigma = 4$).

As discussed in section 5, the equatorial region suffers from spurious large-scale effect of the filtering procedure. For this reason, in the following, the equatorial region (4°S–4°N) is excluded from our analysis.

c. Mean and anomalies

Previous studies based on the same configuration (Jullien et al. 2020; Renault et al. 2020) use a spatial filter to extract mesoscale features. Although a spatial filter can isolate the mesoscale signal better than a temporal filter, it does not have the same properties as a temporal filter. In particular, in a Reynolds decomposition based on a temporal filter, the cross terms are equal to 0 or negligible. This is not the case when using a spatial filter: the cross terms do not disappear. They can be neglected for the wind work (Jullien et al. 2020) but are not necessarily negligible when estimating the baroclinic and barotropic conversion terms. In this study, as detailed below, changes in mesoscale activity are not driven by wind work but rather by a modulation of the conversion terms. For this reason, to have a correct Reynolds decomposition that is needed to estimate these terms, all quantities are decomposed into the seasonal time average defined as the average over each season (January–March, April–June, July–September, and October–December) estimated over the simulated 5-yr period and indicated by an overbar. The deviations from this average are denoted by primes.

d. Eddy kinetic energy

The surface and depth-integrated eddy kinetic energy (EKE; m^2 s^{-2}) is used as a proxy of the intensity of the mesoscale activity. It is computed from the total current anomalies (u, v) estimated as

$$\text{EKE} = \overline{0.5 \left(u'^2 + v'^2\right)}. \tag{1}$$

e. Coupled simulations

Six main 5-yr coupled simulations are performed over the period 1989–93, differing only in the degree of coupling (see also Table 1 for a summary of the window size of the filter in kilometers):

1) In CTRL, NEMO gives WRF hourly averages of SST and surface currents, while the atmospheric model returns hourly averages of freshwater, heat, and momentum (wind stress) fluxes to NEMO. Surface stress is estimated using wind relative to the oceanic current U_{10rel}.
2) The SMTH03 experiment is identical to the CTRL experiment, except that the SST sent to the atmospheric model is smoothed using the spatial Gaussian filter described above with $\sigma = 3$.
3) The SMTH04 experiment is identical to the CTRL experiment, except that the SST sent to the atmospheric model is smoothed using the spatial Gaussian filter described above with $\sigma = 4$. This experiment is the same as SMTH in Renault et al. (2019c) or $C_{\text{CFB\_SMTH}}$ in Renault et al. (2020).
4) SMTH08 is identical to SMTH04 except that the SST sent to the atmospheric model is smoothed using a Gaussian spatial filter with $\sigma = 8$.
5) In SMTH12, the SST sent to the atmospheric model is smoothed using a Gaussian spatial filter with $\sigma = 12$.
6) In NOCFB, the ocean model sends only the SST back to the WRF (without any Gaussian filter). WRF computes the surface stress as a function of the absolute wind at 10 m. NOCFB is used in Renault et al. (2019c), Jullien et al. (2020), and Renault et al. (2020).

As stated in the introduction, TFB has two main direct effects on the low-level atmosphere. On the one hand, as illustrated in Figs. 1a and 1b by the coupling coefficient s_{Cstr} (linear regression coefficient between surface stress curl and cross-
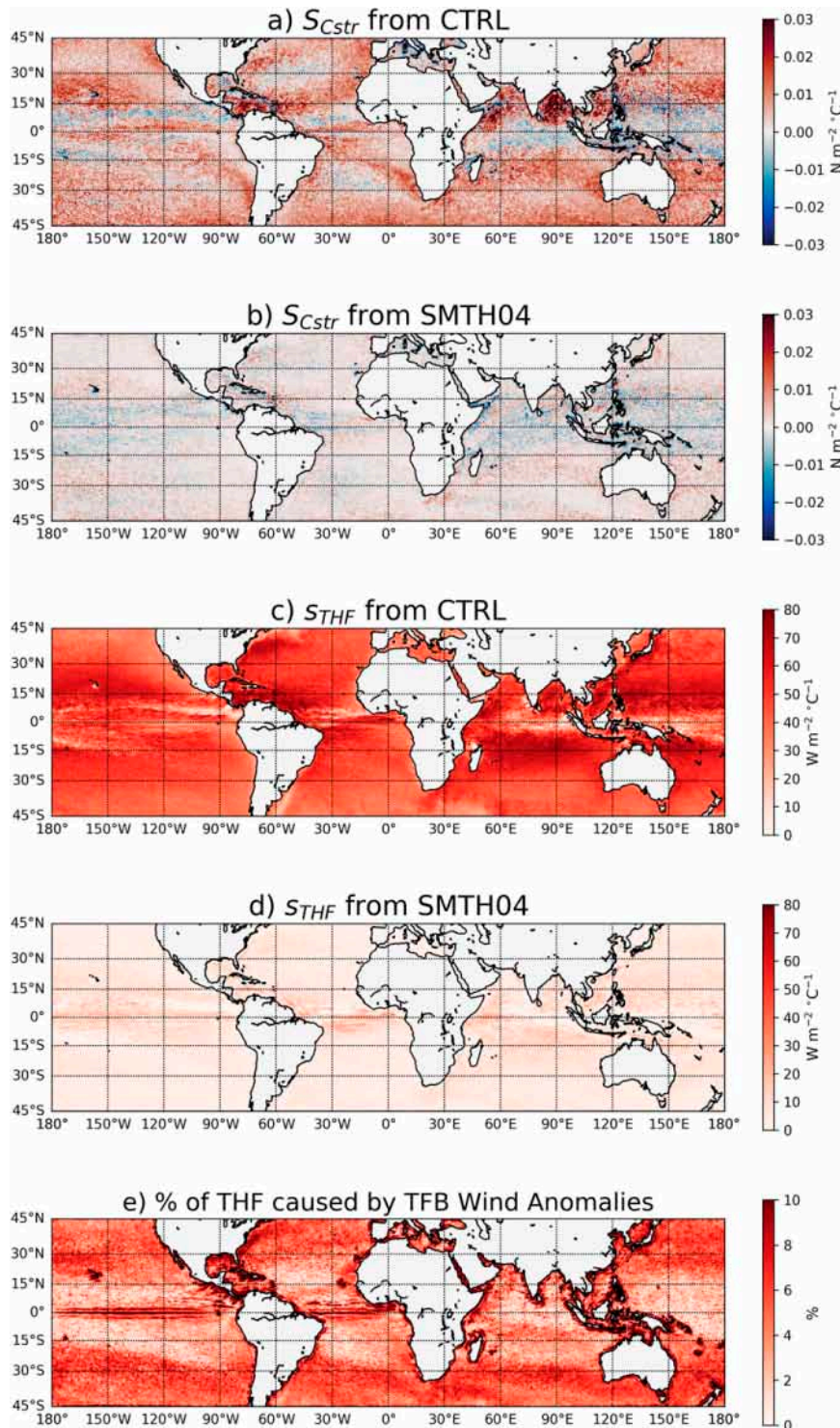
FIG. 1. Direct atmospheric response to the oceanic mesoscale TFB: The wind response is illustrated by the coupling coefficient (s_{Cstr}) between the surface stress curl and the cross-stress SST gradient during summer in each hemisphere from (a) CTRL and (b) SMTH04. The turbulent heat fluxes response is illustrated by the coupling coefficient (s_{THF}) between mesoscale SST and surface turbulent heat flux (THF) anomalies from (c) CTRL and (d) SMTH04. Also shown is (e) the percentage of mesoscale surface turbulent heat fluxes induced by the TFB wind anomalies with respect to the total mesoscale surface THF. See the text for more details.

stress SST gradient; Chelton et al. 2007) for the summer period of each hemisphere from CTRL, it alters the low-level wind and in particular its curl. The atmospheric synoptic variability is first removed using a 29-day running window and anomalies are finally computed using the spatial Gaussian high-pass filter described above with a $\sigma = 4$. The s_{Cstr} can be interpreted as a measure of the surface stress curl response to CFB: the more positive the s_{Cstr} is, the larger the responses of surface stress curl and, thus, TFB-induced Ekman pumping in the ocean will be. Consistent with Chelton et al. (2007) and Renault et al. (2019c), s_{Cstr} is generally characterized by values varying from 0 to 0.01 N m^{-2} °C^{-1}. When the EKE is weak, s_{Cstr} is close to zero, while in regions of intense atmospheric convection (e.g., intertropical convergence zones), atmospheric vortices force the ocean even at the mesoscale, giving rise to negative values of s_{Cstr}. Not surprising, from CTRL to SMTH04, by smoothing the SST seen by the atmosphere, s_{Cstr} is largely reduced, except of course over convective regions where it remains negative (Fig. 1b). The remaining positive values are in fact caused by CFB that contaminates this classic TFB coupling coefficient (Renault et al. 2019c). Similar results are found for the turbulent heat fluxes. To illustrate it, the coupling coefficient between the SST and surface turbulent heat flux (defined positive upward) mesoscale anomalies (defined with a Gaussian filter with $\sigma = 4$ and 29-day running mean) is computed as the slope s_{THF} between their linear regression (Fig. 1c). Consistent with, e.g., Ma et al. (2016), in CTRL, s_{THF} is positive everywhere and is characterized by larger values over western boundary currents and, for example, the Caribbean Sea. In SMTH04, consistent with the smoothing procedure, s_{THF} becomes very weak (Fig. 1d). The surface turbulent heat fluxes (THF) is the sum of the latent (Q_{lat}) and sensible (Q_{sen}) heat fluxes estimated using a bulk formula (Fairall et al. 2003) as

$$\text{THF} = Q_{\text{lat}} + Q_{\text{sen}} = \rho L_E\, C_L (U_{10} - u)(Q_2 - Q_s)$$
$$+ \rho C_P C_S (U_{10} - u)(T_2 - \text{SST}), \tag{2}$$

where L_E is the latent heat of evaporation, C_L is the latent heat transfer coefficient, U_{10} is the 10-m wind, Q_2 is the specific humidity of air 2 m above the sea, Q_s is the specific humidity of air at the sea surface, C_P is the specific heat capacity of air, C_S is the sensible heat transfer coefficient, and T_2 is the air temperature at 2 m. Mesoscale turbulent heat fluxes can therefore originate from three sources: the alteration of exchange coefficients, the air–sea temperature difference per se (and actually the specific humidity), and the wind anomalies caused by TFB. As shown by Sroka et al. (2022), the mesoscale anomalies for exchange coefficients are negligible. The surface turbulent heat flux modulation by mesoscale TFB can therefore directly originate from mesoscale air–sea temperature difference, but also indirectly from the wind anomalies caused by TFB. The contribution of the wind anomalies to the mesoscale TFB is estimated as follows. Based on the coupling coefficient between SST anomalies and 10-m wind anomalies [e.g., O'Neill et al. (2012); see also Renault et al. (2019c) for a spatial map using CTRL], a 10-m wind without

wind anomalies induced by TFB is estimated. The surface turbulent heat flux is then estimated offline (and using the same bulk formula) using the original wind and the 10-m wind without wind anomalies induced by TFB. The additional surface turbulent heat flux induced by the wind anomalies is then computed as the difference between them. Figure 1e depicts its contribution to the total mesoscale turbulent heat flux as the ratio (in %) between the RMS of the mesoscale turbulent heat flux caused by the wind anomalies and the RMS of the total mesoscale turbulent heat flux. In general, TFB-induced wind anomalies cause an additional transfer of heat from mesoscale eddies to the atmosphere, but they remain a second-order mechanism. In some regions, such as the western boundary currents or the equatorial region (i.e., where mesoscale activity is greatest), they can account for up to 10% of the total mesoscale surface heat flux.

To assess the sensitivity of the results to internal ocean variability, as in Renault et al. (2020), two additional coupled simulations identical to CTRL are run on different machines and using different optimization compiler options (CTRL2 and CTRL3). This adds very small perturbations throughout the simulation. This set of three "identical" coupled simulations defines a small ensemble that is used to provide an estimate of the robustness of the results and the role of internal model variability. Note that, because of the small number of experiments, the internal variability is likely underestimated. Unless indicated, the results presented in the following are larger than the internal variability.

3. Damping of the mesoscale activity

To assess the extent to which TFB modulates the mesoscale activity, the surface eddy kinetic energy (EKE) of the different experiments is estimated using seasonal perturbations of surface currents. The spatial distribution of the CTRL surface EKE is shown in Fig. 2a. Consistent with the literature, the largest EKE (>2000 cm^2 s^{-2}) is located above the western boundary currents, the eastern boundary currents have relatively strong EKE (100 < EKE < 400 cm^2 s^{-2}) in comparison with their vicinity, and the center of the gyres is characterized by a weak mesoscale activity (<50 cm^2 s^{-2}).

Figure 2b shows the average difference in surface EKE (excluding the equatorial region) between CTRL and SMTH12, while Fig. 3a plots the mean, median, and 95% percentile of surface EKE for each simulation. As in Renault et al. (2020), the 95% percentile is chosen to represent western boundary currents. While the spatial EKE patterns of CTRL and SMTH12 (and the other smoothed simulations) are very similar (not shown), from CTRL to SMTH12, the surface EKE increases particularly over the Kuroshio, Agulhas Return Current, Malvinas Current, and to some extent along the eastern boundary currents (Peru–Chile, Benguela, Senegal, and Australia) except for California, which is consistent with Seo et al. (2016). This reveals that the mesoscale TFB (defined using a $\sigma = 12$) leads to a damping of the surface mesoscale activity, which is in agreement with Ma et al. (2016). The mean and median surface EKE of the domain increase by about 12% and by ∼10% over western boundary currents (where the EKE is largest). Note that these
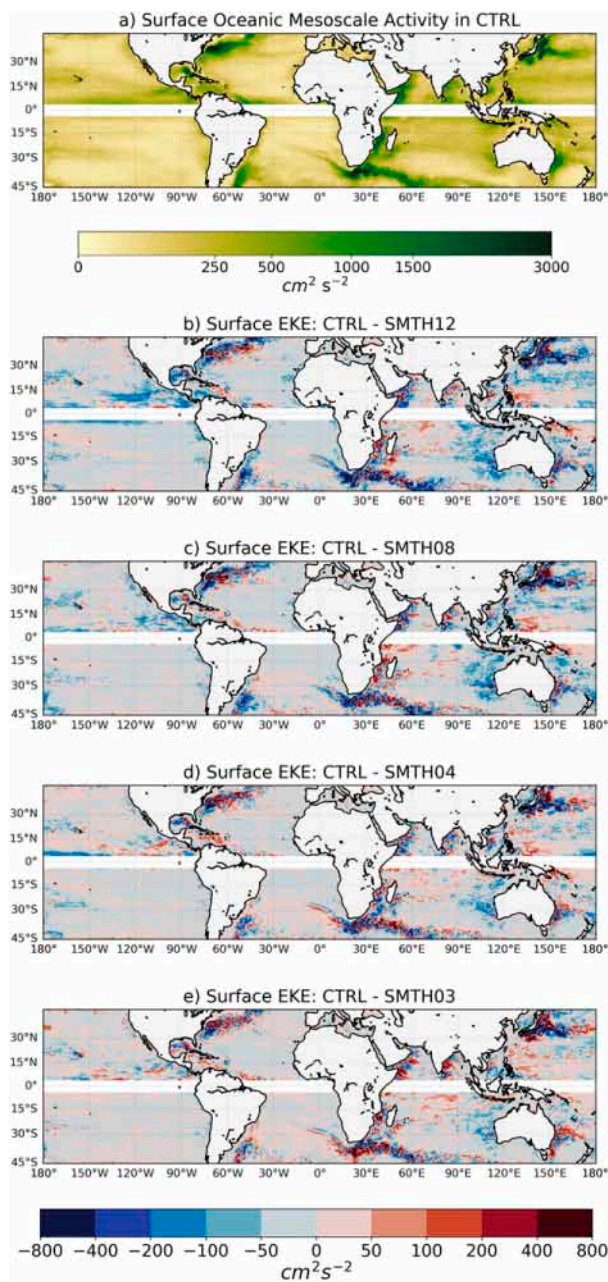
FIG. 2. Mean sea surface EKE and its modulation by mesoscale TFB: (a) Sea surface EKE from CTRL, and sea surface EKE difference between CTRL and (b) SMTH12, (c) SMTH08, (d) SMTH04, and (e) SMTH03.

differences are larger than the internal variability ($\approx 2\%$, estimated from the ensemble, not shown).

To have a sense of the sensitivity of the mesoscale activity modulation by TFB to the spatial filter used, the surface EKE is further estimated from the SMTH08, SMTH04, and SMTH03 experiments. The average differences in surface EKE between CTRL and these simulations are shown in Figs. 2c and 2d. By decreasing the spatial filter cutoff, the increase of the EKE is reduced and becomes more subtle in general. The lower the SST

smoothing, the smaller the EKE increase. On average, the surface EKE increases by about 4%, 8%, and 12% from CTRL to SMTH04, SMTH08, and SMTH12, respectively, while from CTRL to SMTH03, it remains roughly the same. Similar values are found for the median and over western boundary currents. Ma et al. (2016) suggested a stronger damping of the mesoscale activity at smaller scales (less than 100 km). To test this hypothesis, we also estimated the EKE from the simulations using various spatial filters instead of a temporal filter. We found that the EKE damping by TFB is similar whatever the scales used in the spatial filter (not shown).

Mesoscale TFB can therefore damp to some extent the surface EKE directly or by means of a change in the large-scale atmospheric circulation. The strength of the damping strongly depends on how the mesoscale SST anomalies felt by the atmosphere are filtered. To better understand the extent to which TFB affects the mesoscale activity, the mean vertical profile of the EKE is furthermore estimated for CTRL and the other simulations over the whole domain and over the regions that represent the 95% percentile (Figs. 3b,c). Not surprising, at depth, down to 500 m, while the spatial distribution of the EKE is generally similar to that of the surface EKE, its intensity weakens. Consistent with the previous results, the mesoscale TFB can cause a damping of the EKE that depends on the filter cutoff. Over all of the domain, the EKE simulated in STMH03 and SMTH04 are similar than that in CTRL, however, the comparison between SMTH08 or SMTH12 and CTRL reveals a damping of the EKE down to 200 m: the 200-m depth-integrated EKE is increased by 2.6% and 6.1% from CTRL to SMTH08 and to SMTH12, respectively. The EKE damping by is more evident when focusing on western boundary currents (Fig. 3c) except for when comparing SMTH03 to CTRL. From CTRL to SMTH04, SMTH08, and SMTH12, the depth-integrated EKE over the first 200 m is increased by 7.5%, 4.4%, and 3.2% respectively. Beyond 200-m depth, the damping of mesoscale activity becomes more subtle, even when comparing CTRL with SMTH12.

To conclude this section, mesoscale TFB can damp the mesoscale activity. However, this damping is mainly concentrated in the first 200 m depth and its strength appears to be highly dependent on the smoothing scale chosen to remove the mesoscale SST signal felt by the atmosphere. While a too small filter cutoff may underestimate the strength of the TFB damping (e.g., in SMTH03), a too large cutoff (such as that of SMTH12) may not only smooth the mesoscale signal but also part of the large-scale meridional SST gradients, modifying the wind and altering the mean circulation. This will be illustrated in section 5.

4. Mechanisms at work

In this section, a simplified Lorenz cycle is calculated to diagnose the processes that lead to the reduction in EKE revealed in the previous section. Focus is done on four main terms: the eddy windwork (F_eK_e), the barotropic energy conversion (K_mK_e), the baroclinic energy conversion (P_eK_e), and the mesoscale exchange of potential energy between the
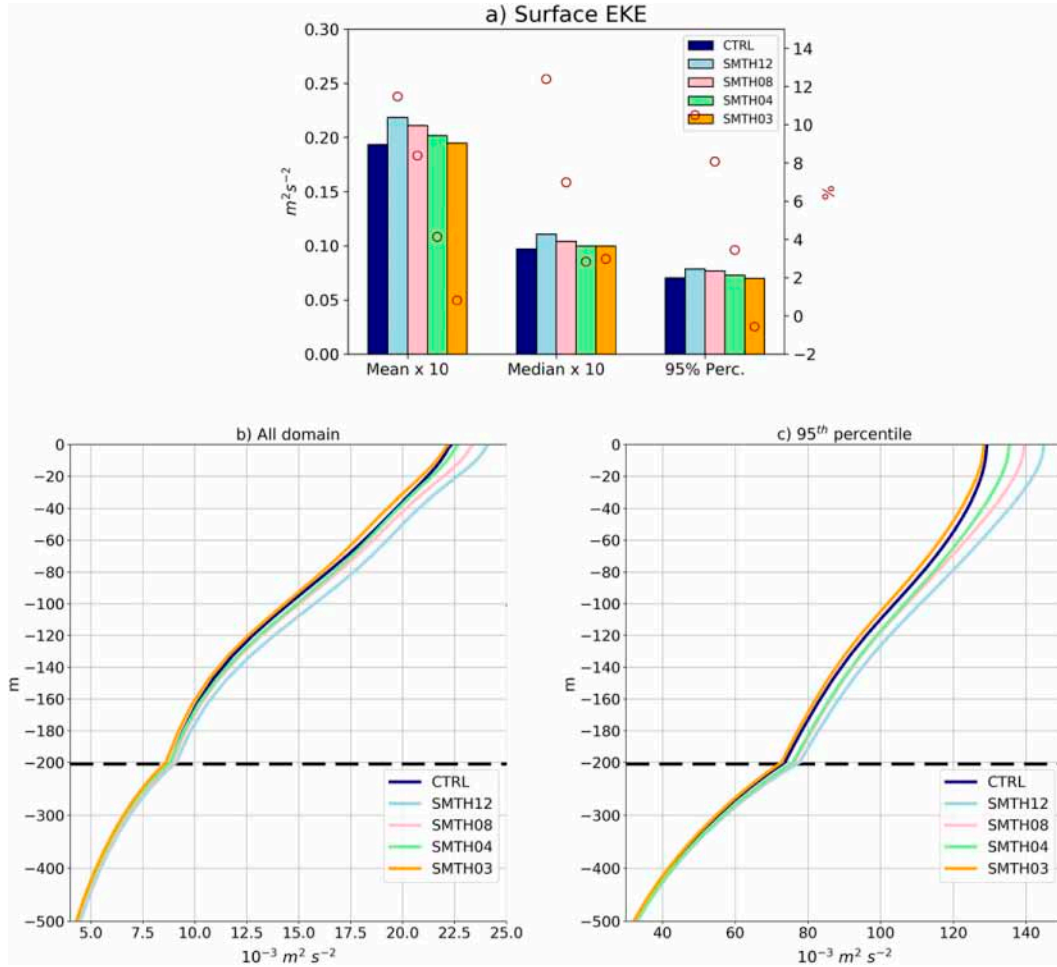
FIG. 3. (a) Main statistics of surface EKE. The 95% percentile of the distribution roughly corresponds to western boundary currents. The red circles indicate the percent of increase from CTRL to another simulation. Also shown are the vertical profiles of the EKE averaged (b) over all of the domain and (c) over the region corresponding to the 95% percentile of the distribution. TFB causes a damping of the EKE mainly at the surface. It strongly depends on the filter cutoff used to smooth out the mesoscale SST seen by the atmosphere.

ocean and atmosphere (GPe), which directly constrains the P_eK_e.

a. Eddy windwork

The eddy wind work (F_eK_e, m³ s⁻³) represents the exchange of momentum between oceanic mesoscale currents and the atmosphere. It is defined as

$$F_eK_e = \frac{1}{\rho_0}\left(\overline{\tau'_x U'_{\text{og}}} + \overline{\tau'_y V'_{\text{og}}}\right), \qquad (3)$$

where ρ_0 is the mean seawater density, U_{og} and V_{og} are the zonal and meridional surface geostrophic currents, and τ_y and τ_x are the zonal and meridional surface stresses. Figure 4a represents the spatial distribution of F_eK_e as estimated from CTRL. In agreement with, e.g., Renault et al. (2017a, 2020), in CTRL F_eK_e is negative almost everywhere, except along the coasts where wind perturbations cause an offshore Ekman

surface current and an oceanic coastal jet (e.g., Renault et al. 2009) that partially flows in the same direction as the wind. The negative values express the energy sinks induced by CFB and the so-called eddy killing phenomenon that leads to a reduction in mesoscale activity of about 30%.

Comparisons of the simulations reveal that F_eK_e decreases by approximately 5%, 4%, 2%, and less than 1% from CTRL to SMTH12, SMTH08, SMTH04, and SMTH03, respectively (not shown). Accordingly, filtering out the mesoscale TFB should therefore cause an increase of the EKE rather than a damping. Such a modulation of F_eK_e is actually a symptom of the damping of the EKE by TFB rather than a cause. Renault et al. (2016b) define the coupling coefficient s_τ between the surface current vorticity and the surface stress curl. s_τ can be interpreted as the efficiency of CFB: the more negative s_τ is, the more efficient the eddy killing will be. Following Renault et al. (2017b), the sink of energy induced by CFB can approximately be defined as the product between s_τ and the EKE.
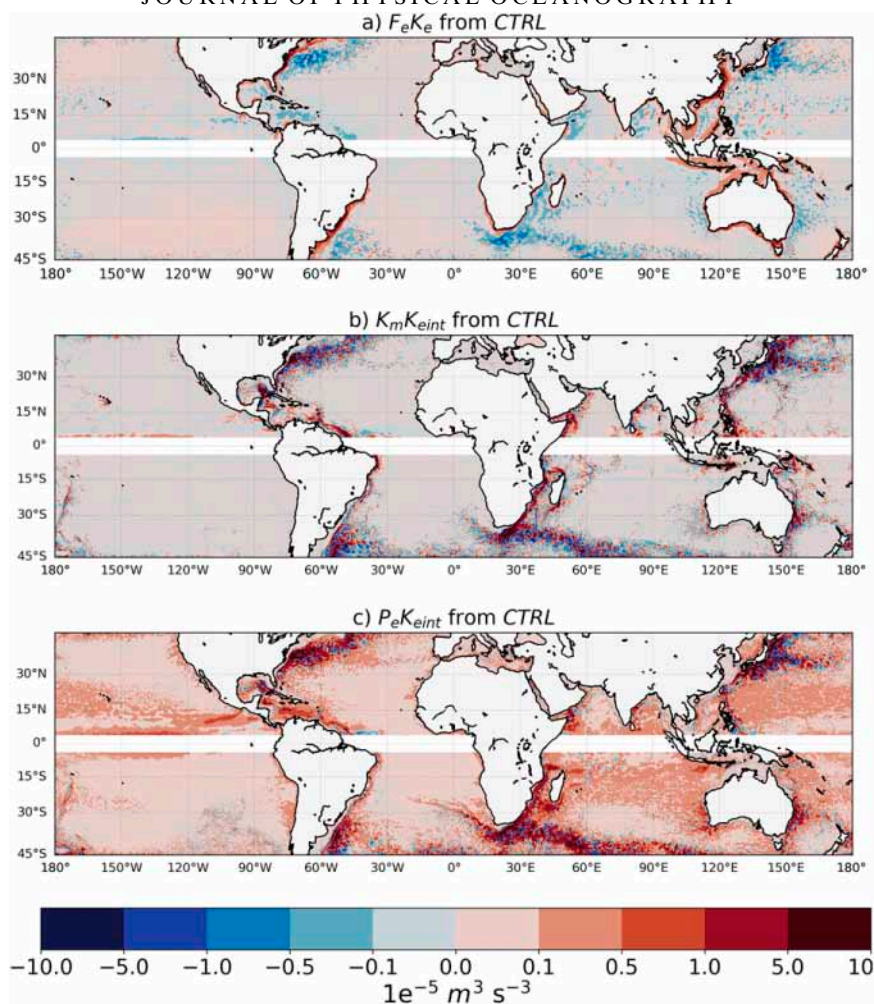
FIG. 4. Main terms of energy conversion and eddy windwork from CTRL: (a) F_eK_e, (b) K_mK_{eint}, and (c) P_eK_{eint}.

Consistent with Renault et al. (2019c), s_τ remains roughly the same between the simulations as it is barely impacted by the TFB surface stress curl induced anomalies (Renault et al. 2019c). Therefore, the reduction of the surface EKE by TFB causes logically a weakening of F_eK_e.

b. Barotropic and baroclinic conversion

Expression K_mK_e represents the barotropic conversion from mean kinetic energy to EKE and is estimated as

$$K_mK_e = -\left(\overline{u'u'}\frac{\partial \overline{u}}{\partial x} + \overline{u'v'}\frac{\partial \overline{u}}{\partial y} + \overline{u'w'}\frac{\partial \overline{u}}{\partial z} \right.$$
$$\left. + \overline{v'u'}\frac{\partial \overline{v}}{\partial x} + \overline{v'v'}\frac{\partial \overline{v}}{\partial y} + \overline{v'w'}\frac{\partial \overline{v}}{\partial z} \right), \quad (4)$$

where w is the vertical velocity and x, y, and z are the zonal, meridional, and vertical coordinates, respectively. The integral of K_mK_e over the water column is then estimated as $K_mK_{eint} = \int_z K_mK_e$.

Expression P_eK_e represents the baroclinic conversion from eddy available potential energy to EKE and is estimated as

$$P_eK_e = \overline{w'b'}, \quad (5)$$

with b is the buoyancy and w is the vertical velocity. The integral of P_eK_e over the water column is then estimated as $P_eK_{eint} = \int_z P_eK_e$; K_mK_e and P_eK_e are estimated using the 5-day average 3D outputs from the simulations over the whole water column.

The spatial distributions of K_mK_{eint} and P_eK_{eint} from CTRL are shown in Figs. 4b and 4c, and Figs. 5 and 6 represent the boxplots of K_mK_{eint} and P_eK_{eint} using the different simulations as well as the vertical profile of K_mK_{eint} and P_eK_{eint} averaged over the whole domain and over the regions that correspond to the 95% percentile. In agreement with the literature, K_mK_{eint} is larger along western boundary currents and their extensions. P_eK_{eint} is generally positive and, as expected, is larger over the most eddying regions such as western and eastern boundary currents. P_eK_{eint} is generally the main driver of EKE generation, except along the Somali and Brazilian currents where K_mK_{eint} dominates.
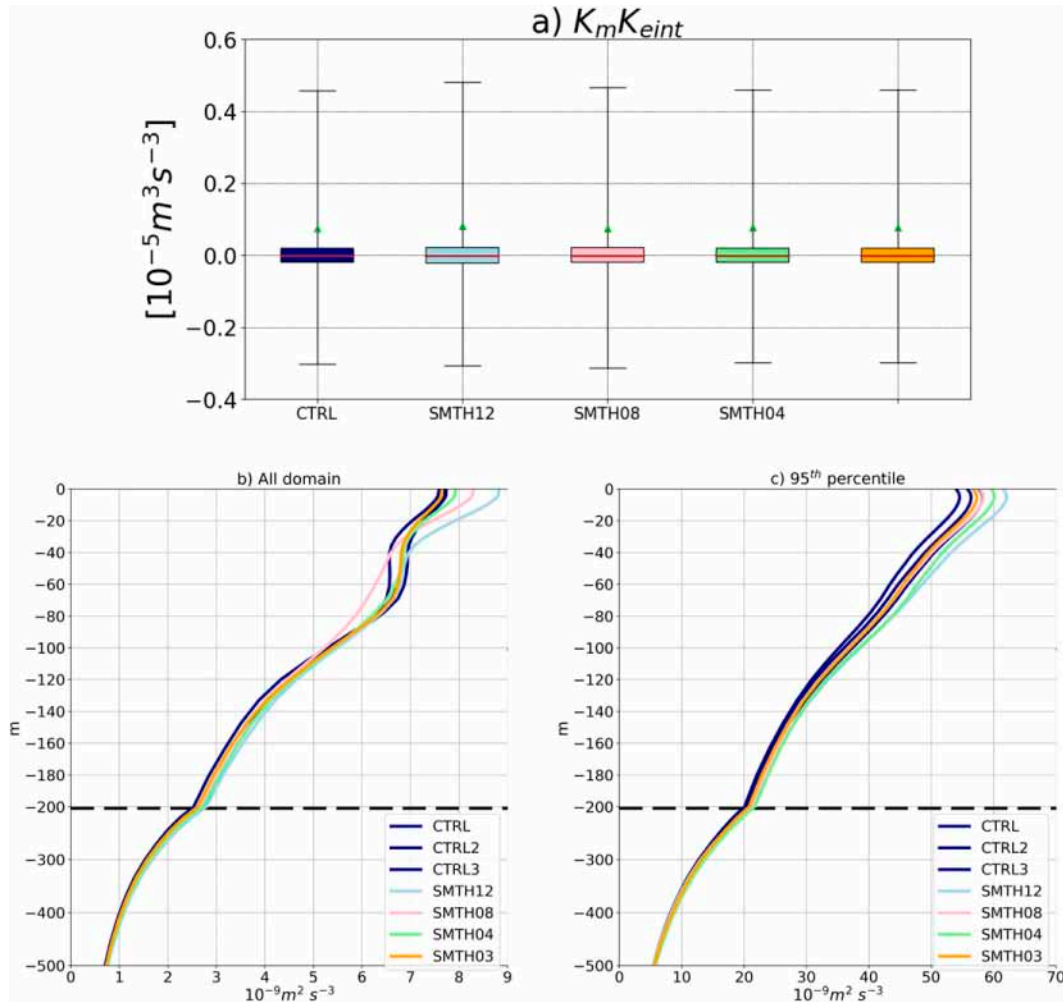
FIG. 5. TFB has a weak impact on the barotropic conversion of energy: (a) Boxplot of $K_m K_{eint}$. As in Renault et al. (2020), the line that divides the box into two parts represents the median of the data, whereas the green dot represents its mean. The length of the box shows the upper and lower quartiles. The extreme lines represent the 95th percentiles of the distributions. (b) Vertical profile of $K_m K_e$ averaged over the whole domain. As highlighted by the black dashed line, a zoom is done over the first 200 m of depth. (c) As in (b), but averaged over the region corresponding to the 95% percentile of the distribution.

Smoothing the SST seen by the atmospheric model has a weak to very weak effect on $K_m K_{eint}$ depending on the filter cutoff. Focusing on the surface layers or over western boundary currents does not really make a large difference (Fig. 5). For instance, differences in $K_m K_e$ averaged over the whole domain (excluding 4°S–4°N) are not significant below 40-m depth and are otherwise weak. Over western boundary currents, only the differences from SMTH12 to CTRL are significant, but they remain weak (less than 3% over the first 100 m of depth). Therefore, the damping of SST by TFB does not act through a reduction of the barotropic conversion of energy neither.

In agreement with Ma et al. (2016), TFB affects the baroclinic conversion of energy, as revealed by a modulation of the mean and median of $P_e K_{eint}$ in Fig. 6a. As with the EKE, the alteration of $P_e K_{eint}$ depends strongly on the filter cutoff:

the larger the spatial filter cutoff used in the simulations, the more positive $P_e K_{eint}$. The mesoscale TFB damps the EKE by partly preventing the generation of eddies by $P_e K_{eint}$, i.e., by reducing the transfer of potential energy to eddy kinetic energy.

Analysis of the vertical profile of the baroclinic conversion over the first 500 m of depth provides a better understanding of how mesoscale TFB can affect the EKE. Consistent with the EKE damping, the effect of TFB on $P_e K_e$ is more pronounced near the surface, both when averaging over the whole domain and over western boundary currents. Baroclinic conversion of energy gradually increases everywhere from CTRL to SMTH03, SMTH04, SMTH08, and SMTH12, although the increases from CTRL to SMTH03 and SMTH04 are more subtle, but they remain significant because they are larger than the difference between CTRL, CTRL2, and
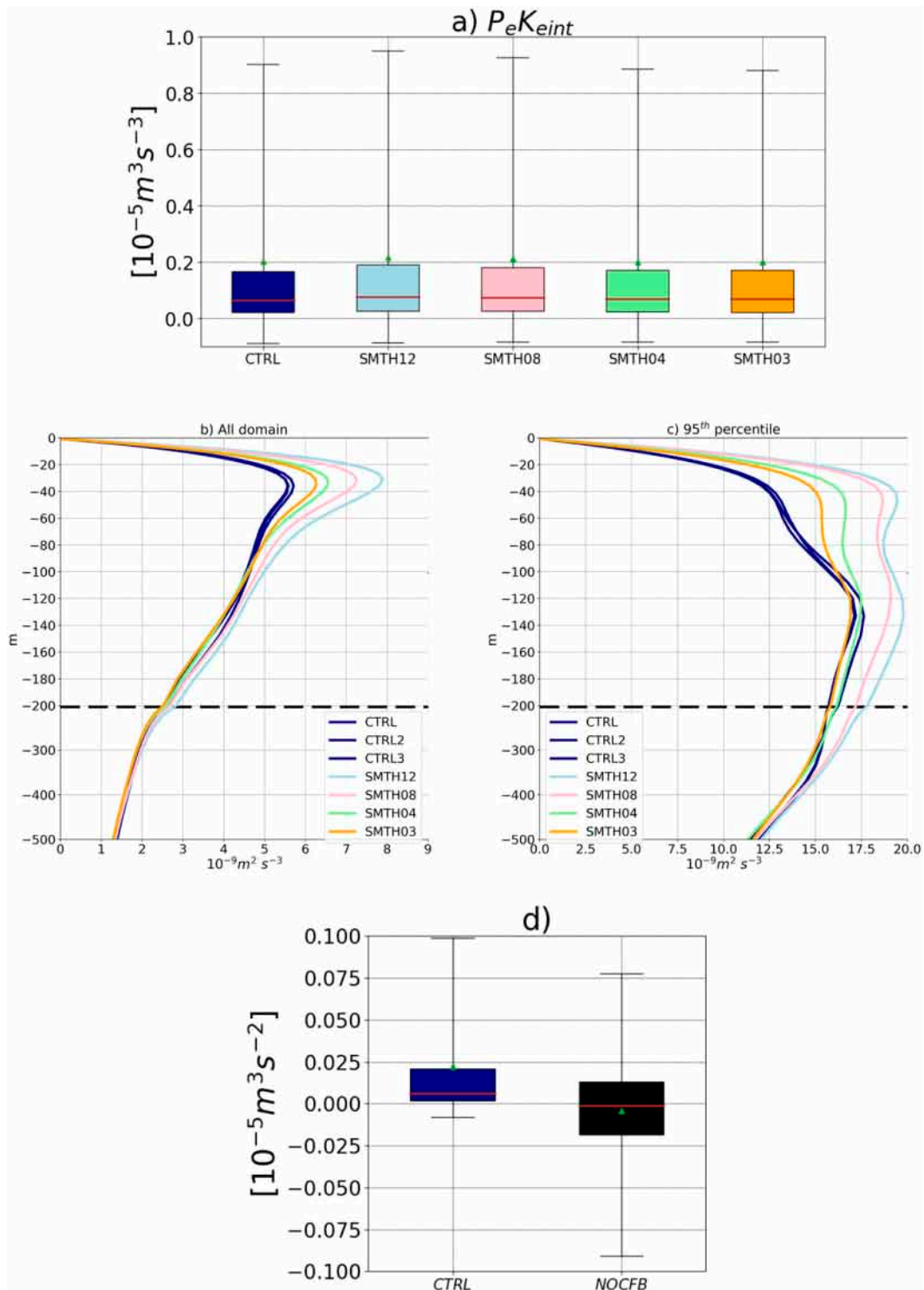
FIG. 6. (a)–(c) As in Fig. 5, but for the baroclinic conversion of energy. (d) Boxplot $P_eK_{e\_OA\_ekman}$ from CTRL and NOCFB. TFB causes a reduction of the conversion of potential energy to kinetic energy by baroclinic instability, explaining the damping of the EKE. The TFB-induced Ekman pumping velocities do not cause additional baroclinic conversion of energy.

CTRL3. Over western boundary currents, that is, where the signal is the strongest, from CTRL to SMTH12 P_eK_e difference can reach up to 50% at 40-m depth but only up to 16% from CTRL to SMTH03, which is again significant with respect to the differences between CTRL, CTRL2, and CTRL3. Again, beyond 200-m depth, differences are not significant.

c. Sink of potential energy induced by TFB

Difference in baroclinic conversion can be explained by a modulation of both w' and b'. On the one hand, both TFB and CFB induce surface stress curl anomalies $\tau'_{OA} = \tau'_{TFB} + \tau'_{CFB}$ (e.g., Fig. 1 for TFB) that cause an additional Ekman pumping w'_{OA_ekman} (Chelton et al. 2007; Renault et al. 2016b). For the sake of simplicity and to estimate an upper bound of the importance of Ekman pumping induced by TFB and CFB in explaining the EKE damping, a constant Ekman pumping is considered over the first 50 m of depth. This assumption is very simplistic and has many caveats because it considers a constant depth of the Ekman layer, a constant viscosity, and does not take into account the variation of Ekman pumping along the water column by considering vertical Ekman velocities equal to the maximum value suggested by Ekman (1905):

$$w'_{OA\_ekman} = \frac{1}{f}\nabla \times \tau'_{OA}. \tag{6}$$

The upper bound of baroclinic instability induced by the Ekman pumping can furthermore be estimated as

$$P_eK_{e\_OA\_ekman} = \int_{z=50} \overline{w'_{ekman} b'} . \tag{7}$$

In CTRL, $P_eK_{e\_OA\_ekman}$ appears as a second-order mechanism in the generation of EKE by baroclinic instabilities, representing less than 4% of the total P_eK_e (Fig. 6d). Note that this value is likely to be overestimated for the caveats mentioned above. Because this estimate contains both TFB and CFB contributions, to unravel them $P_eK_{e\_OA\_ekman}$ is furthermore estimated from NOCFB, that is, a simulation that neglects CFB and, thus, the CFB-induced Ekman pumping. By contrast, in NOCRT, the boxplot of $P_eK_{e\_OA\_ekman}$ is centered around zero, with random positive and negative values around it (Fig. 6d). This reveals that the TFB-induced surface stress and the subsequent induced Ekman pumping are not spatially coherent with the buoyancy anomalies. It does not cause a significant additional baroclinic conversion of energy. This is somehow consistent with Gaube et al. (2015) and Oerder et al. (2018) that show that the Ekman pumping (linear and nonlinear) induced by TFB has a dipole pattern, which nullifies its impact once averaged over the eddy.

On the other hand, mesoscale TFB can affect buoyancy by extracting freshwater and cooling to relatively light water masses and by adding freshwater and heating to relatively heavy water masses, which control the increase of baroclinic conversion in the first 200 m. Following von Storch et al. (2012) and Bishop et al. (2020), the sink of available potential energy by mesoscale TFB is estimated as the rate of available potential energy generation by the transient SST and net air–sea heat and freshwater flux:

$$\text{GPe} = -\frac{1}{\rho}\left(\int_S g\frac{\alpha_{o,1}}{n_o}\overline{\rho' J'_s} - g\frac{\beta_{o,1}}{n_o}\overline{\rho' G'_s}\, dS\right), \tag{8}$$

where $\alpha_{o,1}$ and $\beta_{o,1}$ are values of expansion coefficients in the uppermost model layer, $J_s = H/(\rho C)$ and $G_s = \text{S1}(E - P)$ are respectively the temperature and salinity fluxes at the sea surface, $C = 4000$ J (kg K)$^{-1}$ is the specific heat of seawater, H is the total heat flux at the sea surface, S1 is the time-mean salinity in the uppermost model layer, E is the evaporation rate and P is the precipitation rate at the sea surface.

Figure 7a represents the spatial distribution of GPe from CTRL. GPe is globally positive with large negative values over the most eddying regions such as the western boundary currents (<-5 mW m^{-2}). Smoothing the SST from CTRL to SMTH12 removes the large negative values and leads to an overall increase of GPe everywhere. On average, from CTRL to SMTH12, GPe increases from 0.04 to 0.16 mW m^{-2}. However, consistent with the previous results, the modulation of GPe is sensitive to the filter cutoff used in the simulations. From CTRL to SMTH03, SMTH04, and SMTH08, GPe increases by 0.05, 0.1, and 0.14 mW m^{-2}, respectively, and most of the negative values over western boundary currents are removed in SMTH03, except that of the Agulhas Current, likely because it is characterized by larger eddies. Note that Bishop et al. (2020) show the presence of sink of potential energy from the ocean to the atmosphere (i.e., a negative GPe) everywhere over the World Ocean. Such a result can be retrieved by using a 91-day window (or a spatial filter, not shown) that better separates the transient SST from the seasonal signal, leading to a negative GPe in CTRL almost everywhere. However, the differences between the simulations are similar, pointing to a removal of potential energy from the ocean to the atmosphere induced by mesoscale TFB.

To sum up, in agreement with Ma et al. (2016), the turbulent heat fluxes induced by TFB cause a sink of potential energy through GPe, which is responsible for a damping of buoyancy anomalies, for associated reduction of P_eK_e and, hence, for the EKE damping. However, the sink of potential energy, and the subsequent reduction of P_eK_e and EKE depend strongly on the cutoff of the filter used.

5. On the large-scale effect of the filter cutoff

Ma et al. (2016) show a large impact of mesoscale TFB on the Kuroshio characteristics using a global model (and a 1000-km filter cutoff) but a reduced impact using a regional model (see their Figs. 2g,h). To assess the extent to which mesoscale TFB affects the mean ocean circulation, the mean depth-integrated kinetic energy is estimated from the simulations. In our simulations, the impact of the TFB on the western boundary currents is not clear. Large differences between CTRL and the smoothed experiments are visible over these regions (Figs. 8b–e) but their amplitude is comparable to the difference between CTRL and CTRL2 (Fig. 8a), suggesting that the signal is mostly related to the internal variability and can hardly be explained by the TFB.
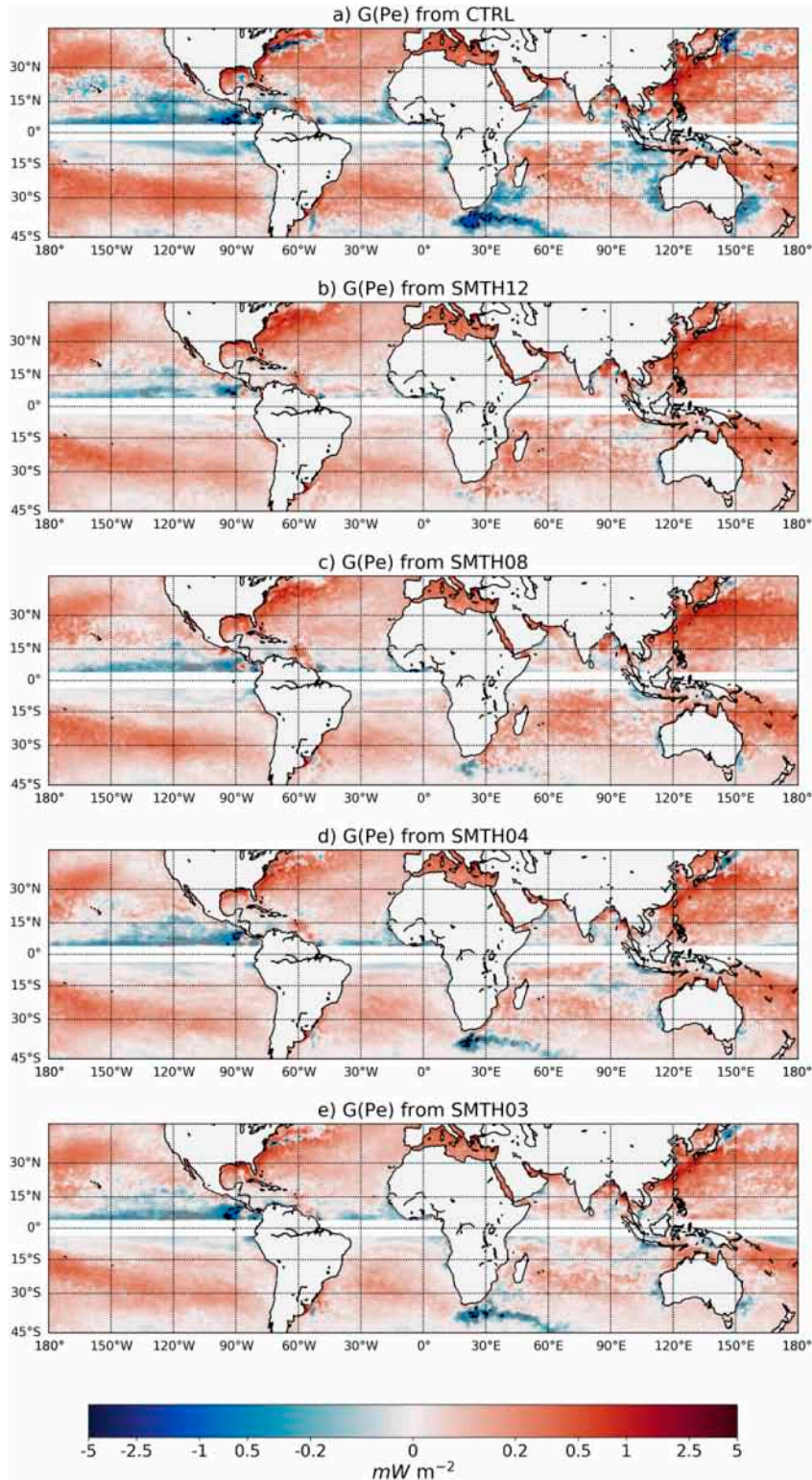
FIG. 7. Sink of eddy available potential energy induced by mesoscale TFB. Smoothing out the SST seen by the atmosphere removes the sink of potential energy caused by eddies. Again, there is a strong dependence on the filter cutoff used.
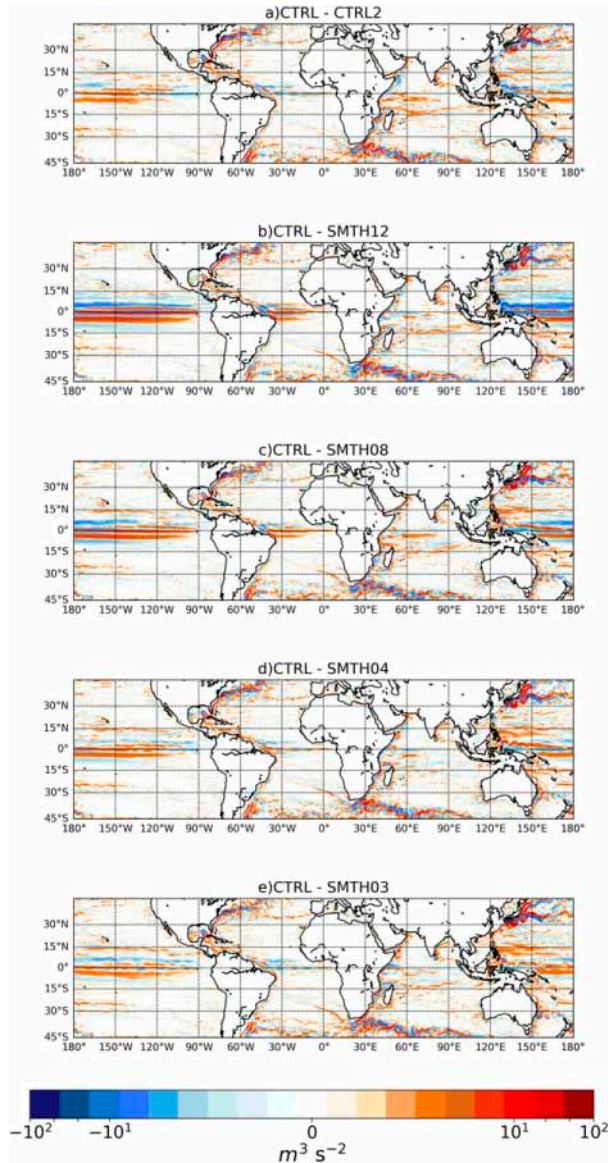
FIG. 8. Depth-integrated mean kinetic energy difference between CTRL and the SST-smoothed simulations.

However, comparison between CTRL and SMTH12 (Fig. 8) reveals that the smoothing of the SST seen by the atmosphere largely affects the mean equatorial circulation, with difference much larger than the internal variability (Fig. 8a). The entire meridional structure of the surface currents is impacted and, as a result, the mean zonal current is modulated by about 0.2 m s^{-1} (not shown).

It could be argued that the large-scale impact is a rectified or indirect effect of the mesoscale response to TFB. However, on the one hand, as shown in section 3, the EKE is only slightly sensitive to TFB. On the other hand, the smoothing procedure can cause spurious effects, especially on the surface stress curl. Indeed, too large of a filter can smooth not only eddies and fronts, but also large-scale SST gradients and sea
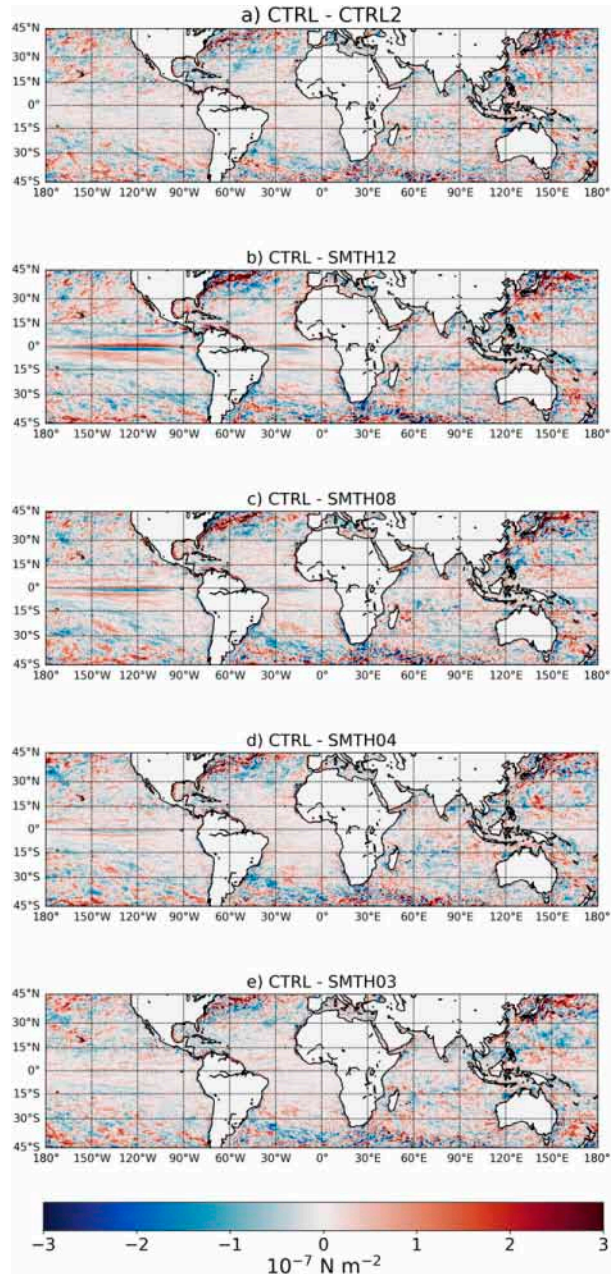

FIG. 9. Mean stress curl difference between CTRL and the SST-smoothed simulations.

ice cover in a global model, which in turn can influence the mean surface stress curl. Figure 9 shows the mean stress curl difference between CTRL and the other simulations, including a perturbed CTRL simulation (CTRL2). Comparison of CTRL and SMTH12 reveals that a filter with a $\sigma = 12$ causes a dramatic change in the mean wind stress curl that is much larger than the internal variability. This effect is mitigated by reducing the filter cutoff, but it remains present (and larger than the internal variability) with, for example, a $\sigma = 8$ filter in SMTH08. As shown by, e.g., Kessler et al. (2003),

Sun et al. (2019, 2021), the representation of the equatorial current structure in an ocean model is very sensitive to the mean surface stress curl. Any change in the large-scale surface stress curl can therefore affect the current structure and subsequently the energy conversion by baroclinic and barotropic instabilities. The equatorial region should be assessed using a zonal filter that preserves the meridional gradients; however, this is out of the scope of this study.

6. Summary and discussion

Seo et al. (2016), for the California Current, suggest that mesoscale TFB does not alter the intensity of mesoscale activity but rather disrupts eddy propagation. In contrast, Ma et al. (2016), focusing on the Kuroshio, argue that mesoscale TFB, by inducing a sink of eddy available potential energy from the ocean to the atmosphere, modulates the oceanic mesoscale activity by more than 20%. Both studies use online spatial smoothing to filter out the mesoscale signal from the SST as seen by the atmosphere. However, Seo et al. (2016) considers a 300-km low-pass filter as opposed to a 1000-km low-pass filter in Ma et al. (2016) in their global configuration. In this study, using a realistic subtropical channel centered on the equator (45°S–45°N) domain for ocean–atmosphere coupled simulation, we aim to determine the extent to which the mesoscale TFB damps the mesoscale ocean activity as well as the sensitivity of the results to the cutoff filter used to smooth out the mesoscale SST signal sent to the atmospheric model. We show that, on average, the mesoscale TFB damps the oceanic mesoscale activity over the first 200 m of depth. The damping is more pronounced over western boundary currents. However, such a damping depends strongly on the cutoff used to filter the mesoscale SST sent to the atmosphere. Using a $\sigma = 12$ cutoff, the surface mesoscale activity increases by an average of 12%. The increase becomes more subtle when reducing the filter cutoff, or even not significant with a cutoff of $\sigma = 3$.

In agreement with Ma et al. (2016), we first confirm that TFB-induced damping is primarily due to induced heat fluxes anomalies. TFB-induced heat fluxes alter ocean buoyancy by extracting freshwater and cooling from relatively light water masses, and vice versa. By filtering the SST seen by the atmosphere, we show that the sinks of eddy available potential energy vanish, explaining the increase of mesoscale activity. TFB also induces surface stress curl anomalies, and thus additional Ekman pumping. However, its contribution to the baroclinic instability is negligible because the induced Ekman pumping anomalies are not coherent with anomalies of buoyancy, which is consistent with (Gaube et al. 2015; Oerder et al. 2018). Last, when neglecting TFB, the absence of sink of potential energy from the ocean to the atmosphere is partly compensated by a more negative a windwork, that is, a larger sink of momentum from the ocean to the atmosphere, which results in a more pronounced eddy killing.

SST filtering must be done carefully, as the filtering procedure can significantly modify the large-scale meridional SST gradients, with major implications on the mean state of air–sea coupled simulations. If this happens, the SST smoothing will potentially create large differences in the sensitivity

experiments related to the rectification of the coupled model mean state and not to the SST mesoscale structure. We show for example that when using a cutoff filter of $\sigma = 8$, the equatorial surface stress curl is largely altered, which modifies the mean equatorial dynamics with major consequences on the model results with no links to the SST mesoscale anomalies. Depending on the region, a zonal filter may be applied to preserve large-scale meridional SST gradients.

Are we doomed to use coupled ocean–atmosphere models or at least an ocean–atmosphere boundary layer model (as, e.g., Lemarié et al. 2021), or can we use existing parameterizations or develop new ones? Following the results of this study, TFB damping of mesoscale activity, which occurs through a modification of the ocean buoyancy, is likely to be taken into account in a forced ocean model by the bulk formula. The bulk formula allows estimating turbulent fluxes associated with SST anomalies, although such damping may be slightly erroneous for two main reasons. On the one hand, by essence, because of the highly nonlinear (sub)mesoscale dynamics, there is a high probability that the modeled SST and the prescribed atmospheric forcing will not be consistent. This would, depending on the eddy imprint seen by the atmosphere, lead to an over- or underestimation of turbulent fluxes. On the other hand, a bulk formula does not reproduce the wind response to TFB that can be responsible for up to 10% of the turbulent fluxes response to TFB. Nonetheless, given the relatively small impact of the TFB on the mesoscale activity, we suggest that such discrepancies may be neglected. The SST damping may also be sensitive to the bulk formulae used in the model (here Fairall et al. 2003) as shown by, for example, Brodeau et al. (2017) and Bonino et al. (2022). At the submesoscales, currents are characterized with scales of 10^2–10^4 m horizontally, 10–100 m vertically, and from hours to days temporally. Submesoscale currents drive vertical velocities one or two orders of magnitude larger than those associated with mesoscale currents and are associated with intense fronts. The effect of TFB at those scales may be different and should therefore be assessed using a similar method as that from this study.

Data availability statement. Data can be downloaded online (https://figshare.com/s/374c96dc0ca373ea1949).

REFERENCES

Betts, A., and M. Miller, 1986: A new convective adjustment scheme. Part II: Single column tests using GATE wave, BOMEX, ATEX and arctic air-mass data sets. *Quart. J. Roy. Meteor. Soc.*, **112**, 693–709, https://doi.org/10.1002/qj.49711247308.

Bishop, S. P., R. J. Small, and F. O. Bryan, 2020: The global sink of available potential energy by mesoscale air-sea interaction. *J. Adv. Model. Earth Syst.*, **12**, e2020MS002118, https://doi.org/10.1029/2020MS002118.

Blanke, B., and P. Delecluse, 1993: Variability of the tropical Atlantic Ocean simulated by a general circulation model with two different mixed-layer physics. *J. Phys. Oceanogr.*, **23**, 1363–1388, https://doi.org/10.1175/1520-0485(1993)023<1363: VOTTAO>2.0.CO;2.

Bonino, G., D. Iovino, L. Brodeau, and S. Masina, 2022: The bulk parameterizations of turbulent air–sea fluxes in NEMO4: The origin of sea surface temperature differences in a global model study. *Geosci. Model Dev.*, **15**, 6873–6889, https://doi.org/10.5194/gmd-15-6873-2022.

Brodeau, L., B. Barnier, A.-M. Treguier, T. Penduff, and S. Gulev, 2010: An ERA40-based atmospheric forcing for global ocean circulation models. *Ocean Modell.*, **31**, 88–104, https://doi.org/10.1016/j.ocemod.2009.10.005.

——, ——, S. K. Gulev, and C. Woods, 2017: Climatologically significant effects of some approximations in the bulk parameterizations of turbulent air–sea fluxes. *J. Phys. Oceanogr.*, **47**, 5–28, https://doi.org/10.1175/JPO-D-16-0169.1.

Bye, J. A. T., 1985: Large-scale momentum exchange in the coupled atmosphere-ocean. *Coupled Ocean-Atmosphere Models*, J. C. J. Nihoul, Ed., Elsevier Oceanography Series, Vol. 40, Elsevier, 51–61.

Chelton, D. B., and S.-P. Xie, 2010: Coupled ocean-atmosphere interaction at oceanic mesoscales. *Oceanography*, **23**, 52–69, https://doi.org/10.5670/oceanog.2010.05.

——, and Coauthors, 2001: Observations of coupling between surface wind stress and sea surface temperature in the eastern tropical Pacific. *J. Climate*, **14**, 1479–1498, https://doi.org/10.1175/1520-0442(2001)014<1479:OOCBSW>2.0.CO;2.

——, M. G. Schlax, M. H. Freilich, and R. F. Milliff, 2004: Satellite measurements reveal persistent small-scale features in ocean winds. *Science*, **303**, 978–983, https://doi.org/10.1126/science.1091901.

——, ——, and R. M. Samelson, 2007: Summertime coupling between sea surface temperature and wind stress in the California Current system. *J. Phys. Oceanogr.*, **37**, 495–517, https://doi.org/10.1175/JPO3025.1.

Chen, F., and J. Dudhia, 2001: Coupling an advanced land surface–hydrology model with the Penn State–NCAR MM5 modeling system. Part I: Model implementation and sensitivity. *Mon. Wea. Rev.*, **129**, 569–585, https://doi.org/10.1175/1520-0493(2001)129<0569:CAALSH>2.0.CO;2.

Chou, M.-D., and M. J. Suarez, 1999: A solar radiation parameterization for atmospheric studies. NASA Tech. Memo. NASA/TM-1999-104606, Vol. 15, 38 pp., http://gmao.gsfc.nasa.gov/pubs/docs/Chou136.pdf.

Cornillon, P., and K.-A. Park, 2001: Warm core ring velocities inferred from NSCAT. *Geophys. Res. Lett.*, **28**, 575–578, https://doi.org/10.1029/2000GL011487.

Craig, A., S. Valcke, and L. Coquart, 2017: Development and performance of a new version of the OASIS coupler, OASIS3-MCT_3.0. *Geosci. Model Dev.*, **10**, 3297–3308, https://doi.org/10.5194/gmd-10-3297-2017.

Czaja, A., C. Frankignoul, S. Minobe, and B. Vannière, 2019: Simulating the midlatitude atmospheric circulation: What might we gain from high-resolution modeling of air-sea interactions? *Curr. Climate Change Rep.*, **5**, 390–406, https://doi.org/10.1007/s40641-019-00148-5.

Dee, D., and Coauthors, 2011: The ERA-Interim reanalysis: Configuration and performance of the data assimilation system. *Quart. J. Roy. Meteor. Soc.*, **137**, 553–597, https://doi.org/10.1002/qj.828.

Desbiolles, F., B. Blanke, A. Bentamy, and N. Grima, 2014: Origin of fine-scale wind stress curl structures in the Benguela and Canary upwelling systems. *J. Geophys. Res. Oceans*, **119**, 7931–7948, https://doi.org/10.1002/2014JC010015.

——, ——, ——, and C. Roy, 2016: Response of the Southern Benguela upwelling system to fine-scale modifications of the coastal wind. *J. Mar. Syst.*, **156**, 46–55, https://doi.org/10.1016/j.jmarsys.2015.12.002.

——, R. Blamey, S. Illig, R. James, R. Barimalala, L. Renault, and C. Reason, 2018: Upscaling impact of wind/sea surface temperature mesoscale interactions on southern Africa austral summer climate. *Int. J. Climatol.*, **38**, 4651–4660, https://doi.org/10.1002/joc.5726.

Dewar, W. K., and G. R. Flierl, 1987: Some effects of the wind on rings. *J. Phys. Oceanogr.*, **17**, 1653–1667, https://doi.org/10.1175/1520-0485(1987)017<1653:SEOTWO>2.0.CO;2.

Duhaut, T. H. A., and D. N. Straub, 2006: Wind stress dependence on ocean surface velocity: Implications for mechanical energy input to ocean circulation. *J. Phys. Oceanogr.*, **36**, 202–211, https://doi.org/10.1175/JPO2842.1.

Eden, C., and H. Dietze, 2009: Effects of mesoscale eddy/wind interactions on biological new production and eddy kinetic energy. *J. Geophys. Res.*, **114**, C05023, https://doi.org/10.1029/2008JC005129.

Ekman, V. W., 1905: On the influence of the Earth's rotation on ocean-currents. *Ark. Mat. Astron. Fys.*, **2**, 1–52.

Fairall, C. W., E. F. Bradley, J. E. Hare, A. A. Grachev, and J. B. Edson, 2003: Bulk parameterization of air–sea fluxes: Updates and verification for the COARE algorithm. *J. Climate*, **16**, 571–591, https://doi.org/10.1175/1520-0442(2003)016<0571:BPOASF>2.0.CO;2.

Foussard, A., G. Lapeyre, and R. Plougonven, 2019: Storm track response to oceanic eddies in idealized atmospheric simulations. *J. Climate*, **32**, 445–463, https://doi.org/10.1175/JCLI-D-18-0415.1.

Gaube, P., D. B. Chelton, R. M. Samelson, M. G. Schlax, and L. W. O'Neill, 2015: Satellite observations of mesoscale eddy-induced Ekman pumping. *J. Phys. Oceanogr.*, **45**, 104–132, https://doi.org/10.1175/JPO-D-14-0032.1.

Gruber, N., Z. Lachkar, H. Frenzel, P. Marchesiello, M. Münnich, J. C. McWilliams, T. Nagai, and G.-K. Plattner, 2011: Eddy-induced reduction of biological production in eastern boundary upwelling systems. *Nat. Geosci.*, **4**, 787–792, https://doi.org/10.1038/ngeo1273.

Hong, S.-Y., and J.-O. J. Lim, 2006: The WRF Single-Moment 6-Class Microphysics Scheme (WSM6). *J. Korean Meteor. Soc.*, **42**, 129–151.

——, Y. Noh, and J. Dudhia, 2006: A new vertical diffusion package with an explicit treatment of entrainment processes. *Mon. Wea. Rev.*, **134**, 2318–2341, https://doi.org/10.1175/MWR3199.1.

Hughes, C. W., and C. Wilson, 2008: Wind work on the geostrophic ocean circulation: An observational study of the effect of small scales in the wind stress. *J. Geophys. Res.*, **113**, C02016, https://doi.org/10.1029/2007JC004371.

Janjić, Z. I., 1994: The step-mountain Eta coordinate model: Further developments of the convection, viscous sublayer, and turbulence closure schemes. *Mon. Wea. Rev.*, **122**, 927–945, https://doi.org/10.1175/1520-0493(1994)122<0927:TSMECM>2.0.CO;2.

Jullien, S., S. Masson, V. Oerder, G. Samson, F. Colas, and L. Renault, 2020: Impact of ocean–atmosphere current feedback on the ocean mesoscale activity: Regional variations and sensitivity to model resolution. *J. Climate*, **33**, 2585–2602, https://doi.org/10.1175/JCLI-D-19-0484.1.

Kang, D., and E. N. Curchitser, 2015: Energetics of eddy–mean flow interactions in the Gulf Stream region. *J. Phys. Oceanogr.*, **45**, 1103–1120, https://doi.org/10.1175/JPO-D-14-0200.1.

Kelly, K. A., S. Dickinson, M. J. McPhaden, and G. C. Johnson, 2001: Ocean currents evident in satellite wind data. *Geophys. Res. Lett.*, **28**, 2469–2472, https://doi.org/10.1029/2000GL012610.

Kessler, W. S., G. C. Johnson, and D. W. Moore, 2003: Sverdrup and nonlinear dynamics of the Pacific equatorial currents. *J. Phys. Oceanogr.*, **33**, 994–1008, https://doi.org/10.1175/1520-0485(2003)033<0994:SANDOT>2.0.CO;2.

Kessouri, F., D. Bianchi, L. Renault, J. C. McWilliams, H. Frenzel, and C. A. Deutsch, 2020: Submesoscale currents modulate the seasonal cycle of nutrients and productivity in the California current system. *Global Biogeochem. Cycles*, **34**, e2020GB006578, https://doi.org/10.1029/2020GB006578.

Kirtman, B. P., and Coauthors, 2012: Impact of ocean model resolution on CCSM climate simulations. *Climate Dyn.*, **39**, 1303–1328, https://doi.org/10.1007/s00382-012-1500-3.

Lemarié, F., G. Samson, J.-L. Redelsperger, H. Giordani, T. Brivoal, and G. Madec, 2021: A simplified atmospheric boundary layer model for an improved representation of air–sea interactions in eddying oceanic models: Implementation and first evaluation in NEMO (4.0). *Geosci. Model Dev.*, **14**, 543–572, https://doi.org/10.5194/gmd-14-543-2021.

Luo, J.-J., S. Masson, E. Roeckner, G. Madec, and T. Yamagata, 2005: Reducing climatology bias in an ocean–atmosphere CGCM with improved coupling physics. *J. Climate*, **18**, 2344–2360, https://doi.org/10.1175/JCLI3404.1.

Ma, X., and Coauthors, 2016: Western boundary currents regulated by interaction between ocean eddies and the atmosphere. *Nature*, **535**, 533–537, https://doi.org/10.1038/nature18640.

Madec, G., and NEMO Team, 2015: NEMO ocean engine, version 3.4. Institut Pierre-Simon Laplace Note du Pole de Modélisation 27, 367 pp., https://doi.org/10.5281/zenodo.1464816.

Martin, A. P., and K. J. Richards, 2001: Mechanisms for vertical nutrient transport within a North Atlantic mesoscale eddy. *Deep-Sea Res. II*, **48**, 757–773, https://doi.org/10.1016/S0967-0645(00)00096-5.

McGillicuddy, D. J., and Coauthors, 2007: Eddy/wind interactions stimulate extraordinary mid-ocean plankton blooms. *Science*, **316**, 1021–1026, https://doi.org/10.1126/science.1136256.

McWilliams, J. C., 2008: The nature and consequences of oceanic eddies. *Ocean Modeling in an Eddying Regime*, *Geophys. Monogr.*, Vol. 177, Amer. Geophys. Union, 5–15, https://doi.org/10.1029/177GM03.

Minobe, S., A. Kuwano-Yoshida, N. Komori, S.-P. Xie, and R. J. Small, 2008: Influence of the Gulf Stream on the troposphere. *Nature*, **452**, 206–209, https://doi.org/10.1038/nature06690.

Mlawer, E. J., S. J. Taubman, P. D. Brown, M. J. Iacono, and S. A. Clough, 1997: Radiative transfer for inhomogeneous atmospheres: RRTM, a validated correlated-k model for the longwave. *J. Geophys. Res.*, **102**, 16663–16682, https://doi.org/10.1029/97JD00237.

Oerder, V., F. Colas, V. Echevin, S. Masson, C. Hourdin, S. Jullien, G. Madec, and F. Lemarié, 2016: Mesoscale SST–wind stress coupling in the Peru–Chile current system: Which mechanisms drive its seasonal variability? *Climate Dyn.*, **47**, 2309–2330, https://doi.org/10.1007/s00382-015-2965-7.

——, ——, ——, ——, and F. Lemarié, 2018: Impacts of the mesoscale ocean-atmosphere coupling on the Peru-Chile ocean dynamics: The current-induced wind stress modulation. *J. Geophys. Res. Oceans*, **123**, 812–833, https://doi.org/10.1002/2017JC013294.

O'Neill, L. W., D. B. Chelton, and S. K. Esbensen, 2003: Observations of SST-induced perturbations of the wind stress field over the southern ocean on seasonal timescales. *J. Climate*, **16**, 2340–2354, https://doi.org/10.1175/2780.1.

——, ——, and ——, 2012: Covariability of surface wind and stress responses to sea surface temperature fronts. *J. Climate*, **25**, 5916–5942, https://doi.org/10.1175/JCLI-D-11-00230.1.

Pacanowski, R., 1987: Effect of equatorial currents on surface stress. *J. Phys. Oceanogr.*, **17**, 833–838, https://doi.org/10.1175/1520-0485(1987)017<0833:EOECOS>2.0.CO;2.

Park, H., D. Lee, W.-P. Jeon, S. Hahn, J. Kim, J. Kim, J. Choi, and H. Choi, 2006: Drag reduction in flow over a two-dimensional bluff body with a blunt trailing edge using a new passive device. *J. Fluid Mech.*, **563**, 389–414, https://doi.org/10.1017/S0022112006001364.

Putrasahan, D. A., A. J. Miller, and H. Seo, 2013: Isolating mesoscale coupled ocean–atmosphere interactions in the Kuroshio extension region. *Dyn. Atmos. Oceans*, **63**, 60–78, https://doi.org/10.1016/j.dynatmoce.2013.04.001.

Renault, L., and P. Marchesiello, 2022: Ocean tides can drag the atmosphere and cause tidal winds over broad continental shelves. *Commun. Earth Environ.*, **3**, 70, https://doi.org/10.1038/s43247-022-00403-y.

——, B. Dewitte, M. Falvey, R. Garreaud, V. Echevin, and F. Bonjean, 2009: Impact of atmospheric coastal jet off central Chile on sea surface temperature from satellite observations (2000–2007). *J. Geophys. Res.*, **114**, C08006, https://doi.org/10.1029/2008JC005083.

——, M. J. Molemaker, J. Gula, S. Masson, and J. C. McWilliams, 2016a: Control and stabilization of the Gulf Stream by oceanic current interaction with the atmosphere. *J. Phys. Oceanogr.*, **46**, 3439–3453, https://doi.org/10.1175/JPO-D-16-0115.1.

——, ——, J. C. McWilliams, A. F. Shchepetkin, F. Lemarié, D. Chelton, S. Illig, and A. Hall, 2016b: Modulation of wind work by oceanic current interaction with the atmosphere. *J. Phys. Oceanogr.*, **46**, 1685–1704, https://doi.org/10.1175/JPO-D-15-0232.1.

——, J. C. McWilliams, and S. Masson, 2017a: Satellite observations of imprint of oceanic current on wind stress by air-sea coupling. *Sci. Rep.*, **7**, 17747, https://doi.org/10.1038/s41598-017-17939-1.

——, ——, and P. Penven, 2017b: Modulation of the Agulhas current retroflection and leakage by oceanic current interaction with the atmosphere. *J. Phys. Oceanogr.*, **47**, 2077–2100, https://doi.org/10.1175/JPO-D-16-0168.1.

——, ——, and J. Gula, 2018: Dampening of submesoscale currents by air-sea stress coupling in the Californian upwelling system. *Sci. Rep.*, **8**, 13388, https://doi.org/10.1038/s41598-018-31602-3.

——, F. Lemarié, and T. Arsouze, 2019a: On the implementation and consequences of the oceanic currents feedback in ocean-atmosphere coupled models. *Ocean Modell.*, **141**, 101423, https://doi.org/10.1016/j.ocemod.2019.101423.

——, P. Marchesiello, S. Masson, and J. C. McWilliams, 2019b: Remarkable control of western boundary currents by eddy killing, a mechanical air-sea coupling process. *Geophys. Res. Lett.*, **46**, 2743–2751, https://doi.org/10.1029/2018GL081211.

——, S. Masson, V. Oerder, S. Jullien, and F. Colas, 2019c: Disentangling the mesoscale ocean-atmosphere interactions. *J. Geophys. Res. Oceans*, **124**, 2164–2178, https://doi.org/10.1029/2018JC014628.

——, ——, T. Arsouze, G. Madec, and J. C. McWilliams, 2020: Recipes for how to force oceanic model dynamics. *J. Adv. Model. Earth Syst.*, **12**, e2019MS001715, https://doi.org/10.1029/2019MS001715.

——, T. Arsouze, and J. Ballabrera-Poy, 2021: On the influence of the current feedback to the atmosphere on the western Mediterranean Sea dynamics. *J. Geophys. Res. Oceans*, **126**, e2020JC016664, https://doi.org/10.1029/2020JC016664.

Samson, G., S. Masson, F. Durand, P. Terray, S. Berthet, and S. Jullien, 2017: Roles of land surface albedo and horizontal resolution on the Indian summer monsoon biases in a coupled ocean–atmosphere tropical-channel model. *Climate Dyn.*, **48**, 1571–1594, https://doi.org/10.1007/s00382-016-3161-0.

Seo, H., A. J. Miller, and J. R. Norris, 2016: Eddy–wind interaction in the California current system: Dynamics and impacts. *J. Phys. Oceanogr.*, **46**, 439–459, https://doi.org/10.1175/JPO-D-15-0086.1.

——, and Coauthors, 2023: Ocean mesoscale and frontal-scale ocean–atmosphere interactions and influence on large-scale climate: A review. *J. Climate*, **36**, 1981–2013, https://doi.org/10.1175/JCLI-D-21-0982.1.

Shchepetkin, A. F., and J. C. McWilliams, 2009: Correction and commentary for "ocean forecasting in terrain-following coordinates: Formulation and skill assessment of the regional ocean modeling system" by Haidvogel et al., J. Comp. Phys. 227, pp. 3595–3624. *J. Comput. Phys.*, **228**, 8985–9000, https://doi.org/10.1016/j.jcp.2009.09.002.

Skamarock, W., and Coauthors, 2008: A description of the Advanced Research WRF version 3. NCAR. Tech. Note NCAR/TN-475+STR, 113 pp., https://doi.org/10.5065/D68S4MVH.

Small, R. J., and Coauthors, 2008: Air–sea interaction over ocean fronts and eddies. *Dyn. Atmos. Oceans*, **45**, 274–319, https://doi.org/10.1016/j.dynatmoce.2008.01.001.

——, K. J. Richards, S.-P. Xie, P. Dutrieux, and T. Miyama, 2009: Damping of tropical instability waves caused by the action of surface currents on stress. *J. Geophys. Res.*, **114**, C04009, https://doi.org/10.1029/2008JC005147.

Sroka, S., A. Czaja, and S. Chakravorty, 2022: Assessing the importance of mesoscale sea-surface temperature variations for surface turbulent cooling of the Kuroshio extension in wintertime. *Quart. J. Roy. Meteor. Soc.*, **148**, 2742–2754, https://doi.org/10.1002/qj.4333.

Stammer, D., 1997: Global characteristics of ocean variability estimated from regional TOPEX/POSEIDON altimeter measurements. *J. Phys. Oceanogr.*, **27**, 1743–1769, https://doi.org/10.1175/1520-0485(1997)027<1743:GCOOVE>2.0.CO;2.

Sun, Z., H. Liu, P. Lin, Y.-h. Tseng, J. Small, and F. Bryan, 2019: The modeling of the North Equatorial Countercurrent in the Community Earth System Model and its oceanic component. *J. Adv. Model. Earth Syst.*, **11**, 531–544, https://doi.org/10.1029/2018MS001521.

——, J. Small, F. Bryan, Y.-h. Tseng, H. Liu, and P. Lin, 2021: The impact of wind corrections and ocean-current influence on wind stress forcing on the modeling of Pacific North Equatorial Countercurrent. *Ocean Modell.*, **166**, 101876, https://doi.org/10.1016/j.ocemod.2021.101876.

von Storch, J.-S., C. Eden, I. Fast, H. Haak, D. Hernández-Deckers, E. Maier-Reimer, J. Marotzke, and D. Stammer, 2012: An estimate of the Lorenz energy cycle for the world ocean based on the 1/10° STORM/NCEP simulation. *J. Phys. Oceanogr.*, **42**, 2185–2205, https://doi.org/10.1175/JPO-D-12-079.1.

Wunsch, C., and D. Stammer, 1995: The global frequency-wavenumber spectrum of oceanic variability estimated from TOPEX/POSEIDON altimetric measurements. *J. Geophys. Res.*, **100**, 24 895–24 910, https://doi.org/10.1029/95JC01783.